Primordial clays on Mars formed beneath a steam or supercritical atmosphere

Kevin M. Cannon[1,2], Stephen W. Parman[1] & John F. Mustard[1]

On Mars, clay minerals are widespread in terrains that date back to the Noachian period (4.1 billion to 3.7 billion years ago)[1–5]. It is thought that the Martian basaltic crust reacted with liquid water during this time to form hydrated clay minerals[3,6]. Here we propose, however, that a substantial proportion of these clays was formed when Mars' primary crust reacted with a dense steam or supercritical atmosphere of water and carbon dioxide that was outgassed during magma ocean cooling[7–9]. We present experimental evidence that shows rapid clay formation under conditions that would have been present at the base of such an atmosphere and also deeper in the porous crust. Furthermore, we explore the fate of a primordial clay-rich layer with the help of a parameterized crustal evolution model; we find that the primordial clay is locally disrupted by impacts and buried by impact-ejected material and by erupted volcanic material, but that it survives as a mostly coherent layer at depth, with limited surface exposures. These exposures are similar to those observed in remotely sensed orbital data from Mars[1–5]. Our results can explain the present distribution of many clays on Mars, and the anomalously low density of the Martian crust in comparison with expectations.

Mars accreted and differentiated rapidly after the Solar System formed[10], and both geophysical modelling and geochemical evidence support the presence of a global magma ocean at this early time[7,11]. As this magma ocean cooled, dissolved H_2O and CO_2 were outgassed, building up a steam or supercritical atmosphere (SSA) tens to hundreds of bars thick[7,8] that could have survived for around 10^7 years (ref. 9) and would have reacted with the first-formed solid crust of Mars[7]. Chemical weathering beneath this atmosphere should have been efficient because of the high chemical activity of H_2O, and because pressure (P)–temperature (T) conditions would have been near or beyond the H_2O critical point. These conditions would have been much hotter for a given pressure than were later hydrologic systems on Mars. Clay minerals formed during this intense weathering episode may be preserved to this day, because Mars did not experience mature, subduction-driven plate tectonics[12] to recycle the altered early crust. Extrusive volcanism and impact-ejected material (basin ejecta) would have acted to bury a primordial clay layer; however, clays would have been remobilized by both impacts and physical weathering to incorporate them into younger, Noachian-aged geologic units.

In order to evaluate water–rock interactions at the crust–SSA interface and below, we reacted synthetic crystalline Martian basalt with H_2O and H_2O–CO_2 mixtures at relevant P–T conditions (see Methods for details). Our results show that the basalt is rapidly and extensively altered to form clay minerals (Fig. 1 and Extended Data Fig. 1), with other minor alteration phases also appearing, including nepheline and portlandite. Clay minerals were formed in experimental conditions near the H_2O critical point in all three phase regions (vapour, liquid and supercritical). We identified clays on the basis of: first, morphology in scanning electron micrographs (Fig. 1b–d); second, vibrational absorptions of metal–OH bonds in visible/near-infrared (VNIR) reflectance spectra between 2,200 nm and 2,400 nm that are

diagnostic of iron/magnesium clays (Fig. 1e, f); and third, X-ray diffraction peaks at d-spacings of 10–14 Å that are characteristic of basal [001] reflections of phyllosilicates (Fig. 1f). A variety of iron-rich, trioctahedral clays formed depending on the P–T conditions and the presence or absence of CO_2. For example, in the liquid-water field, a platy, expanding 12 Å clay formed, consistent with interstratified trioctahdral illite-montmorillonite. In the supercritical H_2O field, a fibrous, non-expanding 10 Å clay formed, consistent with palygorskite. Finally, when CO_2 was added, an expanding 14 Å clay formed in the supercritical field, consistent with trioctahedral montmorillonite or vermiculite. Together these experiments demonstrate that P–T conditions at the crust–SSA interface were highly efficient at weathering basaltic rocks to produce clay minerals. Iron-rich dioctahedral species are the most common types of Martian clays identified by remote sensing[13], with the specific species being controlled by the crystal chemistry of the protolith, by P–T conditions and by any subsequent modification. These dioctahedral species probably did not form directly through aqueous alteration, but instead could have originated as iron-rich trioctahedral clays that were later oxidized[13,14]. Therefore the clays formed in our experiments are plausible precursors of those observed on Mars today.

Primordial clays could have formed at considerable depths beneath the SSA because of porosity in the primary crust. The crustal porosity could have taken the form of large-scale fractures that resulted from early impact bombardment, similar to those seen on the Moon[15], and microporosity that formed following thermal contraction when the primary crust cooled[16]. The pore-closure depth for the Martian megaregolith is estimated to be 10 km (ref. 17), suggesting that the SSA could have created an altered, clay-rich layer with a maximum thickness of around 10 km, depending on the rate at which the porosity was created. Such an early-formed, clay-rich layer on the top of the Martian crust would have been reworked by intensive impact bombardment (such as that which produced the Borealis basin[18]), by the emplacement of extrusive volcanic material (that is, secondary crust), and by physical and chemical weathering.

To explore the fate of a primordial clay layer on Mars, we constructed a parameterized three-dimensional box model that considers the effects of SSA-driven alteration, impact excavation, impact melting, secondary crust emplacement and basal geothermal heating (Fig. 2; see Methods for details). The model spans the first billion years after the crust is likely to have solidified[19] (4.538 billion years ago (Ga) to 3.538 Ga), capturing most of the major geologic activity in the history of Mars. In the reference model (Figs 2 and 3a), we consider a sawtooth, late heavy bombardment (LHB) impact flux (ref. 20; Extended Data Fig. 2), with an imposed lull in the formation of large basins between the Borealis impact and the LHB[21], an initial 3-km-thick clay layer, an SSA lasting for 10^7 years, 10 km of ejecta/melt from the Borealis impact being emplaced instantaneously at 4.5 Ga, and 10 km of extrusive secondary crust being emplaced with an exponentially decaying rate. In additional runs, we model the effects of thicker (Fig. 3b) and thinner (Fig. 3c)

[1]Department of Earth, Environmental and Planetary Sciences, Brown University, Providence, Rhode Island 02912, USA. [2]Department of Physics, University of Central Florida, Orlando, Florida 32816, USA.
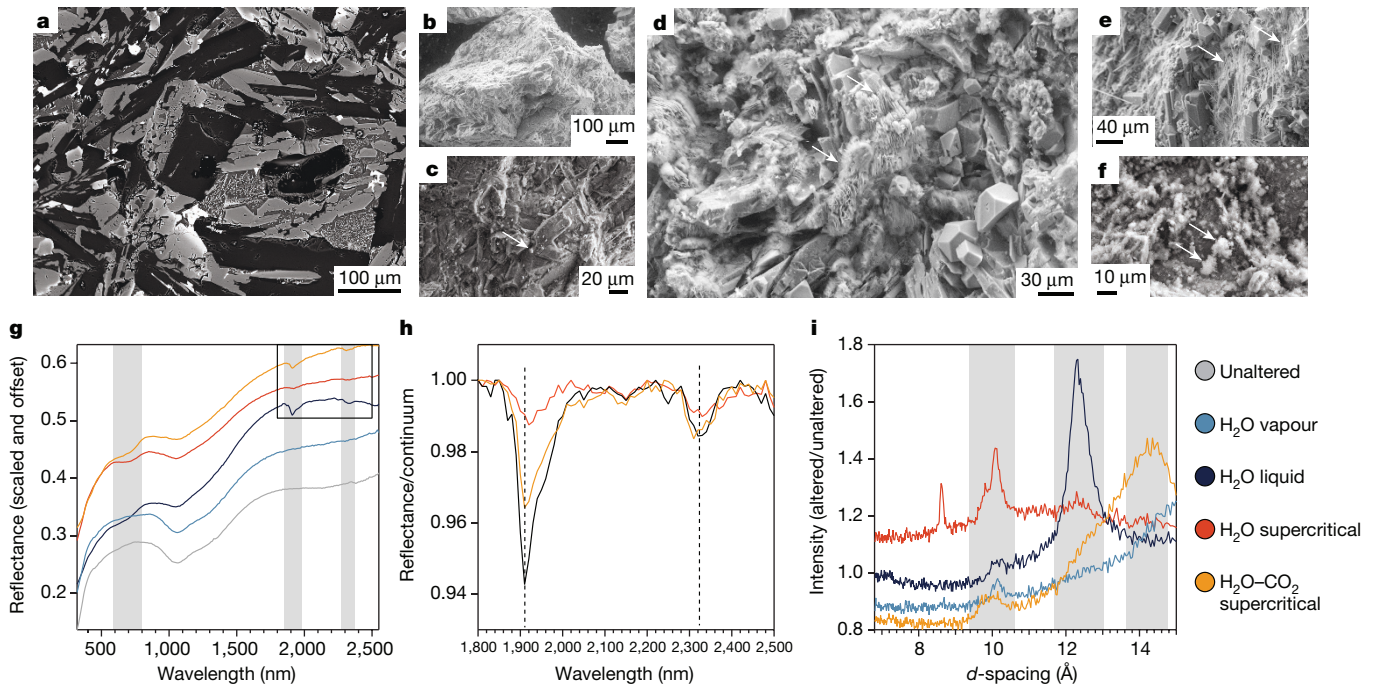
Figure 1 | Analyses of altered basaltic samples. a, Backscatter electron micrograph of a thick section of our unaltered basalt, where from darkest to lightest the phases are: plagioclase; glass (with exsolved bright quench crystals); pyroxene; olivine (zoned); and spinels. **b–f**, Secondary electron images showing the surfaces of unaltered and altered basalt particles. **b**, Unaltered starting basalt **c**, Sample altered at 425 °C and 150 bar (where H_2O is in the form of vapour). **d**, Sample altered at 325 °C and 300 bar (where H_2O is liquid). **e**, Sample altered at 425 °C and 300 bar (where H_2O is in a supercritical state). **f**, Sample altered at 425 °C and 300 bar (with H_2O–CO_2 being in a supercritical state). Arrows point to clay species. **g**, VNIR spectra of unaltered and altered samples, with key absorptions near 700 nm, 1,900 nm and 2,300 nm indicated by grey bars. The box shows the region that is expanded in panel **h**. **h**, VNIR spectra highlighting absorption features near 1,900 nm and 2,300 nm (dotted lines) that are diagnostic of clay minerals. **i**, X-ray diffraction patterns of altered samples, relative to the pattern for unaltered basalt. Characteristic peaks (grey bars) at 10 Å, 12.3 Å and 14 Å represent basal [001] phyllosilicate reflections.

layers of Borealis ejecta, a longer-lasting SSA that persists until the time of the Borealis impact (Fig. 3d), and an accretionary tail impact flux (Fig. 3e). While the SSA is present, we assume that alteration is instantaneous on the 10^5-year time step of the model, and that this alteration extends to a 3-km depth at which porosity rapidly decreases[17].

In all model runs, the primordial clay layer initially thickens while the SSA is present (Fig. 2a). The layer is quickly buried by Borealis melt and ejecta (Fig. 2b), then modified by subsequent impacts and volcanism (Fig. 2c). Changing the model parameters results in different amounts of clay being exposed at the surface, a different overall dilution of the initially pure clay layer, and different burial depths of that layer (Fig. 3 and Extended Data Fig. 3). With twice the reference amount of Borealis cover, there are fewer clay exposures at the surface, and the clay layer is buried much more deeply in the crust (Fig. 3b). The opposite is true of the model with half the reference amount of cover (Fig. 3c). When the SSA lasts for 3.8×10^7 years (until the time of the Borealis impact), the clay layer is less diluted, and shows enhanced surface exposures (Fig. 3d). Finally, using an accretionary tail impact flux results in greater dilution and burial of the clay layer, and a greater clay content in surface materials because of enhanced impact mixing (Fig. 3e). We developed two metrics for evaluating the surface distribution of clays in model runs. The first is the detection rate, defined as the areal fraction of surface grid cells with more than 10% clay (assumed to be detectable by orbital remote sensing). The second is the background clay content, defined as the median clay proportion in surface grid cells outside of detections. The actual areal clay coverage on Mars is estimated to be 3.4% (ref. 4), and the background clay content is probably 1% or less, based on the lack of crystalline clay in soils at Gale crater[22] and in the regolith breccia Northwest Africa 7034, which is a good spectral analogue of typical low-albedo (that is, dust-poor) terrains on Mars[23,24].

Extended Data Fig. 3 shows that two model runs—the reference model and the model with twice the Borealis cover—are consistent with estimates of both of these metrics for Mars. Other model runs predict either too many surface exposures, too much clay in the background regolith, or both.

Our primordial clay model has a number of strengths in explaining observed crustal clay exposures on Mars. In this model, the water and heat needed to drive clay formation are a natural consequence of the Martian magma ocean, and there is no need to appeal to enhanced rainfall, hotter geotherms, or sustained deep groundwater in the younger Noachian period. A primordial clay layer excavated by impacts can explain the patchy distribution of Martian clays, as well a possible clustering of clay detections around the Hellas, Argyre and Isidis basins. These may have been among the small handful of post-Borealis basins[21] that were capable of excavating beneath the thick cover of Borealis ejecta and secondary crust that buried the primordial clay layer. Impact emplacement of older material has been suggested to explain the clays observed deep in the walls of Valles Marineris, which did not form *in situ* as a coherent alteration horizon[25]. Other models for clay formation involve subsurface hydrothermal alteration[3], surficial weathering profiles[6], impact-induced hydrothermal alteration[26], and precipitation directly from magmatic fluids[27]. None of these processes is mutually excluded by the primordial-clay model, but the volume of clays that they contributed might have been limited by the rapid secular cooling of Mars. Observed Martian clays probably contain contributions both from primordial clays formed by the SSA, and from clays formed by these later processes. In many cases it may be difficult to distinguish between the two by using orbital remote sensing alone: *in situ* investigations or returned samples are needed. The SSA would have had a distinct composition from later fluids, which might allow SSA-derived clay to be identified. For example, SSA-derived
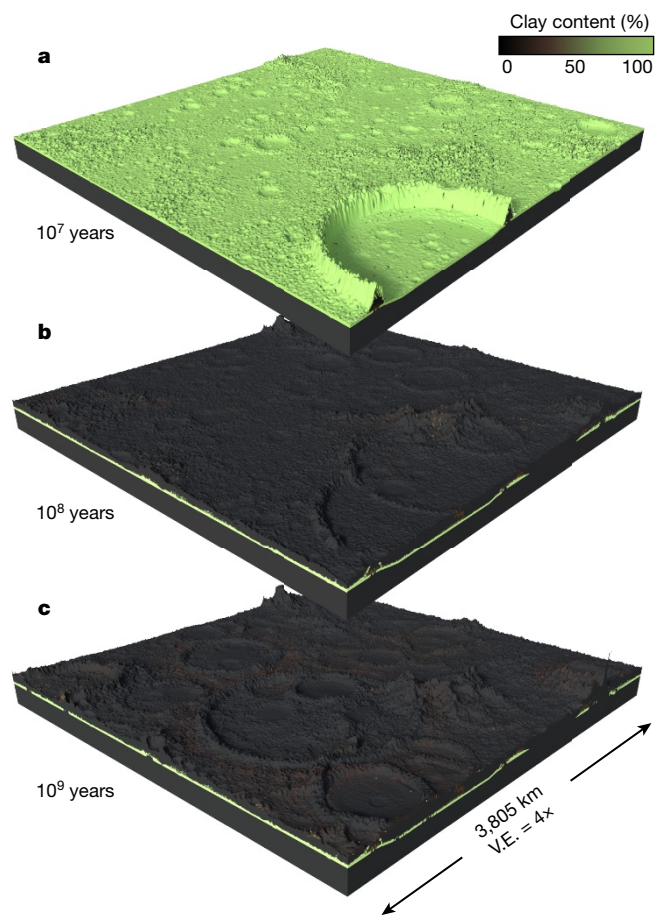
Figure 2 | Results from the reference run of the crustal evolution model. The figure shows perspective views of snapshots from three time steps in the reference model. **a**, After 10^7 years, the initial altered layer has thickened owing to impact-induced excavation of unaltered material. **b**, After 10^8 years, the primordial clay layer is buried by melt and ejecta from the Borealis impact, as well as by extrusive volcanics and other impact melt sheets. **c**, At the end of the model run (10^9 years), the clay-rich layer remains mostly intact at depth; patches of minimally altered rock are exposed at the very surface. V.E., vertical exaggeration.

clay probably has higher noble-gas contents and distinct isotopic compositions compared with later clays. Other volatiles—such as chlorine, fluorine and iodine—may also be useful in distinguishing these clays.

The primordial clay model also has implications for our understanding of early Martian climate, water sequestered in the subsurface, and crustal density. In this model, clay formation is mainly decoupled from the surface climate and is therefore consistent with the mostly cold and dry Noachian conditions suggested by recent three-dimensional climate models[28]. Martian clay minerals are partially hydrated, as indicated by vibrational absorptions from structural and/or adsorbed H_2O and OH^{1-3}. Therefore, a buried clay layer could have sequestered substantial amounts of water in the subsurface of Mars[29] (although both bound and adsorbed water become unstable with increasing pressures and temperatures at depth). A buried primordial clay layer could also explain the anomalously low density of the Martian crust. Topography and crustal density measurements support the presence of a buried low-density layer in the southern highlands crust[30], which is consistent with our modelling results (Fig. 3). Clays were dismissed as a possible contributor to this low-density layer because they were not expected to exist at depths below 1 km (ref. 30), but they have since been discovered at depths of 10 km or more[4]. Similar clay-rich layers formed during magma ocean cooling on Earth and Venus would not be expected to be
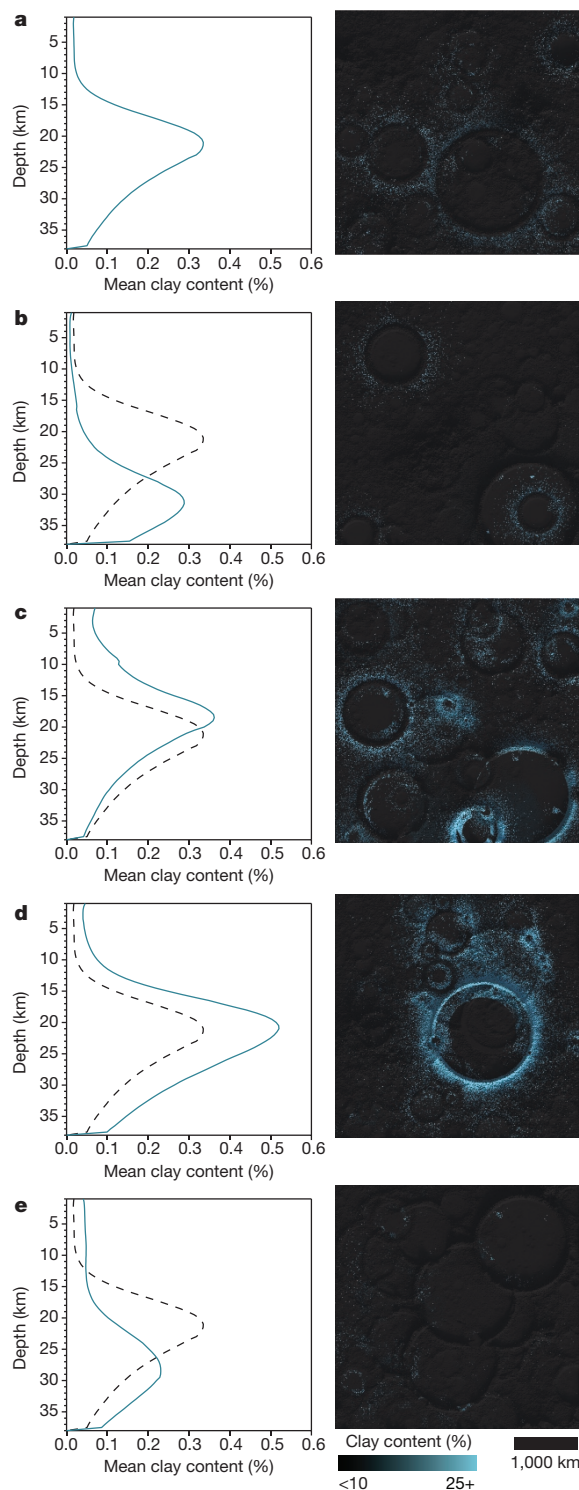

Figure 3 | Alteration profiles and surface exposures for different model parameters. Left-hand plots show the mean clay content as a function of depth at the end of the model runs, with the reference model represented by a grey dashed line in **b**–**e**. Images on the right show a top-down view of the model grid surface, with colours stretched to show smaller clay contents than in Fig. 2. **a**, Reference model (Fig. 2). **b**, Model with 20 km of Borealis material. **c**, Model with 5 km of Borealis material. **d**, Model with SSA lasting for 38 million years, until the time of the Borealis impact (at 4.5 Ga). **e**, Model with accretionary tail impact flux.

preserved at the surface owing to plate tectonics and global resurfacing, respectively, but they might nevertheless have been important to the early geodynamical evolution of those worlds.

1. Bibring, J.-P. *et al.* Mars surface diversity as revealed by the OMEGA/Mars Express observations. *Science* **307,** 1576–1581 (2005).
2. Mustard, J. F. *et al.* Hydrated silicate minerals on Mars observed by the Mars Reconnaissance Orbiter CRISM instrument. *Nature* **454,** 305–309 (2008).
3. Ehlmann, B. L. *et al.* Subsurface water and clay mineral formation during the early history of Mars. *Nature* **479,** 53–60 (2011).
4. Carter, J., Poulet, F., Bibring, J.-P., Mangold, N. & Murchie, S. Hydrous minerals on Mars as seen by the CRISM and OMEGA imaging spectrometers: updated global view. *J. Geophys. Res. Planets* **118,** 831–858 (2013).
5. Sun, V. Z. & Milliken, R. E. Ancient and recent clay formation on Mars as revealed from a global survey of hydrous minerals in crater central peaks. *J. Geophys. Res. Planets* **120,** 2293–2332 (2015).
6. Carter, J., Loizeau, D., Mangold, N., Poulet, F. & Bibring, J.-P. Widespread surface weathering on early Mars: a case for a warmer and wetter climate. *Icarus* **248,** 373–382 (2015).
7. Elkins-Tanton, L. T. Linked magma ocean solidification and atmospheric growth for Earth and Mars. *Earth Planet. Sci. Lett.* **271,** 181–191 (2008).
8. Abe, Y. Physical state of the very early Earth. *Lithos* **30,** 223–235 (1993).
9. Lammer, H. *et al.* Outgassing history and escape of the Martian atmosphere and water inventory. *Space Sci. Rev.* **174,** 113–154 (2013).
10. Dauphas, N. & Pourmand, A. Hf–W–Th evidence for rapid growth of Mars and its status as a planetary embryo. *Nature* **473,** 489–492 (2011).
11. Borg, L. E., Nyquist, L. E., Wiesmann, H., Shih, C.-Y. & Reese, Y. The age of Dar al Gani 476 and the differentiation history of the martian meteorites inferred from their radiogenic isotopic systematics. *Geochim. Cosmochim. Acta* **67,** 3519–3536 (2003).
12. Breuer, D. & Spohn, T. Early plate tectonics versus single-plate tectonics on Mars: evidence from magnetic field history and crust evolution. *J. Geophys. Res. Planets* **108,** 5072 (2003).
13. Michalski, J. R. *et al.* Constraints on the crystal-chemistry of Fe/Mg-rich smectitic clays on Mars and links to global alteration trends. *Earth Planet. Sci. Lett.* **427,** 215–225 (2015).
14. Chemtob, S. M. *et al.* Oxidative alteration of ferrous smectites: a formation pathway for Martian nontronite? *Lunar Planet. Sci. Conf. XLVII,* abstract 2520 (2017).
15. Wieczorek, M. A. *et al.* The crust of the Moon as seen by GRAIL. *Science* **339,** 671–675 (2013).
16. Petford, N. Controls on primary porosity and permeability development in igneous rocks. *Geol. Soc. Spec. Pub.* **214,** 93–107 (2003).
17. Clifford, S. M. A model for the hydrologic and climatic behavior of water on Mars. *J. Geophys. Res. Planets* **98,** 10973–11016 (1993).
18. Marinova, M. M., Aharonson, O. & Asphaug, E. Mega-impact formation of the Mars hemispheric dichotomy. *Nature* **453,** 1216–1219 (2008).
19. Kruijer, T. S. *et al.* The early differentiation of Mars inferred from Hf–W chronometry. *Earth Planet. Sci. Lett.* **474,** 345–354 (2017).
20. Morbidelli, A., Marchi, S., Bottke, W. F. & Kring, D. A. A sawtooth-like timeline for the first billion years of lunar bombardment. *Earth Planet. Sci. Lett.* **355,** 144–151 (2012).
21. Bottke, W. F. & Andrews-Hanna, J. C. A post-accretionary lull in large impacts on early Mars. *Nat. Geosci.* **10,** 344–348 (2017).
22. Bish, D. L. *et al.* X-ray diffraction results from Mars science laboratory: mineralogy of rocknest at Gale Crater. *Science* **341,** 1238932 (2013).
23. McCubbin, F. M. *et al.* Geologic history of Martian regolith breccia Northwest Africa 7034: evidence for hydrothermal activity and lithologic diversity in the Martian crust. *J. Geophys. Res. Planets* **121,** 2120–2149 (2016).
24. Cannon, K. M., Mustard, J. F. & Agee, C. B. Evidence for a widespread basaltic breccia component in the martian low-albedo regions from the reflectance spectrum of Northwest Africa 7034. *Icarus* **252,** 150–153 (2015).
25. Viviano-Beck, C. E., Murchie, S. L., Beck, A. W. & Dohm, J. M. Compositional and structural constraints on the geologic history of eastern Tharsis Rise, Mars. *Icarus* **284,** 43–58 (2017).
26. Tornabene, L. L. *et al.* An impact origin for hydrated silicates on Mars: a synthesis. *J. Geophys. Res. Planets* **118,** 994–1012 (2013).
27. Meunier, A. *et al.* Magmatic precipitation as a possible origin of Noachian clays on Mars. *Nat. Geosci.* **5,** 739–743 (2012).
28. Wordsworth, R. D., Kerber, K., Pierrehumbert, R. T., Forget, F. & Head, J. W. Comparison of "warm and wet" and "cold and icy" scenarios for early Mars in a 3-D climate model. *J. Geophys. Res. Planets* **120,** 1201–1219 (2015).
29. Mustard, J. F. in *Volatiles in the Martian Crust* (Elsevier, 2017).
30. Baratoux, D. *et al.* Petrological constraints on the density of the Martian crust. *J. Geophys. Res. Planets* **119,** 1707–1727 (2014).

METHODS

Basalt synthesis. We synthesized a crystalline basaltic material to use in the alteration experiments. The composition of this sample was based on the bulk chemistry of the meteorite Northwest Africa 7034—a Martian regolith breccia that closely approximates orbital γ-ray spectroscopy data from the bulk crust of Mars[31]. Expressed as wt% oxides, this composition is: 50.57% SiO_2, 13.38% FeO, 11.92% Al_2O_3, 9.5% CaO, 8.31% MgO, 3.98% Na_2O, 1.04% TiO_2, 0.36% K_2O, 0.3% MnO and 0.19% Cr_2O_3. To re-create this composition, we homogenized reagent-grade powders of SiO_2, Fe_2O_3, Al_2O_3, MgO, TiO_2, MnO, Cr_2O_3, $CaCO_3$, K_2CO_3 and Na_2CO_3 under ethanol and then dried them. The resulting powder was decarbonated by heating in a horizontal furnace in air for 3 hours at 950 °C. Approximately 2 g of decarbonated powder were loaded into a 2 ml cylindrical alumina crucible and melted in a horizontal gas-mixing furnace; the sample was first heated to 1,400 °C, above its liquidus, for 2 hours, and then cooled at 5 °C per hour to 1,000 °C, at which point the furnace was shut off and the sample removed and broken out of the crucible. A controlled mixture of CO_2 and CO in the furnace was used to set the oxygen fugacity to 1 logarithmic unit below the quartz–fayalite–magnetite solid oxygen buffer. The mineralogy of the resulting synthetic rock consisted of plagioclase > pyroxene (mostly homogenous at $Wo_{46}En_{30}Fs_{24}$) > olivine (zoned from Fo_{31} to Fo_{63}) with accessory oxides and quenched glass (Fig. 1).

Alteration experiments. The synthetic basaltic rock was ground and dry-sieved to a 0.5–1-mm grain size, then washed with ethanol to remove clinging fines. Aliquots of this particulate sample were loaded in silver–palladium tubing and crimped at both ends, but not welded shut. Samples were then loaded into hydrothermal vessels attached to a water reservoir. The pressure vessels were run in a horizontal furnace. Experiments were run for two weeks, after which the silver–palladium tubing was opened to remove the samples. Experimental conditions were based on modelled magma ocean cooling pathways for the surface of Mars[7] and included P–T conditions in the liquid field (325 °C, 300 bar), vapour field (425 °C, 150 bar) and supercritical field (425 °C, 300 bar). In order to test the effect of CO_2 on alteration products and extent, we ran a separate experiment at 425 °C and 300 bar with a welded silver–palladium tube filled with 100 mg of oxalic acid, which breaks down to give equal molar proportions of H_2O and CO_2.

Sample analysis. We analysed unaltered starting material and altered materials by using X-ray diffraction (XRD), visible/near-infrared (VNIR) spectroscopy, and both energy-dispersive X-ray spectroscopy (EDS) and wavelength-dispersive spectroscopy (WDS) elemental mapping. All analyses were performed in house at Brown University. Samples were ground and dry-sieved to a 45–75-μm size fraction for both XRD and VNIR spectral measurements. XRD was performed on a Bruker D2 PHASER diffractometer. Initial characterization was done from 5° to 70° 2θ, using a step size of 0.02° and a counting time of 15 s. For clay identification, samples were solvated in ethylene glycol, and heated first to 400 °C and then to 550 °C. After each treatment, XRD measurements were taken from 5° to 13° 2θ, with a counting time of 3 s. Diffraction peaks were identified using the Bruker DIFFRAC.SUITE software package. VNIR spectral measurements were made using the custom-built ultraviolet–visible–near-infrared bidirectional spectrometer at the Reflectance Experiment Laboratory at Brown University[32]. Measurements spanned from 320 nm to 2,600 nm with a 10-nm sampling. Absorption features in the spectra were compared to laboratory measurements of pure phases, and specific attention was paid to the Al–OH, Fe–OH and Mg–OH vibrational absorptions that are diagnostic of phyllosilicate minerals and occur at 2,200 nm, 2,290 nm and 2,320 nm, respectively[33]. Samples were imaged using a LEO 1530 VP ultrahigh-resolution field emitter scanning electron microscope in variable pressure mode with a voltage of 20 kV (Fig. 1b–f). EDS spectra were used to measure the qualitative elemental chemistry of alteration phases. Basalt grains were also mounted in epoxy and polished to create cross-sections that were mapped on a Cameca SX-100 electron microprobe. Elemental mapping of silicon, aluminium, calcium, iron and magnesium was performed with spatial resolution of 1 μm per pixel (Extended Data Fig. 1).

Crustal evolution model. We constructed a parameterized three-dimensional box model in MATLAB to consider the competing effects of impact ejection, impact melting and secondary crust formation on the fate of a thick altered layer at the top of the primary Martian crust. The model consists of $500 \times 500 \times Z$ grid cells, where Z starts at 300 and grows with time as secondary crustal material is added. The horizontal resolution of each cell is 7.61 km and the vertical resolution is 0.5 km, such that the areal extent of the entire grid represents 10% of Mars' surface area. Each grid cell has a continuous value representing its clay content (0%–100%). The model runs from 4.538 Ga to 3.538 Ga, with a 10^5-year time step, encompassing the time period from solidification of the primary crust (estimated to have occurred at about 30 million years or less after Solar System formation[19]) to the cessation of major impact and volcanic events near the end of the Hesperian period.

At each time step, if the SSA is still present then all unaltered material within a certain depth from the surface (that is, the initial depth of the clay layer) is instantly converted to fully altered material. This assumes that alteration is 100% efficient within the 10^5-year time step of the model. How long the SSA persisted is poorly constrained and estimated to be of the order of 10^7 years (ref. 9). We used a value of 1.0×10^7 years for all model runs except one, in which the SSA was assumed to last for 3.8×10^7 years (until the time of the Borealis impact at 4.5 Ga in the model). A linear geothermal gradient of 20 °C per km is imposed, which converts grid cells heated above 750 °C (that is, 37.5 km depth or greater) into unaltered material, representing thermal alteration and degradation of clays. In the first stage of the model (Fig. 2a), the SSA is present and unaltered rock excavated from depth is altered by the SSA. This acts to thicken the clay-rich layer. After the SSA is gone, no additional clay is formed in the model. Unaltered rock accumulates in the upper crust by melting of clay-rich rock from impacts, and by mantle-derived melts erupted at the surface. Impact cratering mechanically mixes both altered and unaltered crustal materials, diluting the clay-rich material and forming a layered volume of serial ejecta blankets and lava that contains an increasing proportion of unaltered rock over time.

Impact craters are generated using a Monte Carlo approach that is based on cratering rates and size–frequency distributions appropriate for Mars. Craters are selected from the following final crater diameters (D_F; all in km): 50, 60, 70, 80, 90, 100, 115, 130, 150, 170, 200, 250, 300, 350, 400, 450, 500, 600, 700, 800, 900, 100, 1,100, 1,200, 1,300, 1,400 and 1,500. The crater size–frequency distribution (CFSD) follows a uniform power-law relation with a −2.2 slope, appropriate for these large diameters[34]. This CFSD determines the relative probability of a crater of a given size being chosen. The total number of craters per time step (that is, the impact flux) is modelled in two ways (Extended Data Fig. 2): using a sawtooth LHB that is caused by a dynamic instability at around 4.1 Ga (ref. 20) and for a single model run (Fig. 3e) a simple exponential decay (that is, an accretionary tail) that is extrapolated from the N_{50} values of the five basins dated in ref. 35. In the LHB runs, we prescribe a lull in large basins ($D_F > 1,000$ km) after the Borealis event[21], then explicitly add a single 1,500-km basin at 3.9 Ga as a proxy for an Isidis/Argyre-type event. Extended Data Table 1 gives an example crater population for the reference model run.

The crater population for each time step is applied in a random order to the grid at randomized locations, such that each crater interacts with the target in succession. For craters, we calculate the diameter of the transient cavity to be $D_{TC} = 6^{0.15} \times D_F^{0.85}$ (ref. 36). Toroidal flow streams of ejecta extend from the point of impact to the edge of the transient cavity with a maximum excavation depth of $0.1 \times D_{TC}$. Grid cells within this torus are categorized into three vertical sections (shallow, intermediate and deep), and the material in each section is homogenized in terms of its clay content. Ejected grid cells are then distributed one at a time outside the crater rim with a random azimuth, and a random distance r is drawn from a probability function with the form $(r/D_F)^{-2.3}$ (ref. 37). The material sourced from the deep part of the ejecta torus is ejected farthest by slightly biasing r for ejected parcels. The shallow-sourced ejecta ends up closest to the crater rim, with the intermediate section in between. Impact melt volumes are calculated as $3.6382 \times 10^{-4} \times D_{TC}^{3.85}$ (ref. 38), and melt is assumed to be a half-sphere (truncated at the top) extending downwards from the point of impact. Grid cells within the melt radius are reduced to a clay content of 0%. Melt within the ejecta flow streams is added to the ejecta, and the remaining melt is then settled at the bottom of the final crater, whose initial (melt-free) void space is calculated as a paraboloid with depth $0.286 \times D_F^{0.582}$ (ref. 39).

Erupted volcanic material is added at each time step as unaltered grid cells to the upper surface of the grid in a fractal-like pattern. The thickness (T) of erupted volcanic material, averaged over the grid, diminishes with time as a simple exponential function, $T = A \times \exp(-bt)$, where A is the initial volumetric crustal production rate at $t = 0$ (20 km^3 per year; ref. 40), distributed evenly over the grid; b is fixed by the total erupted thickness over the model duration; and t is time. The total volume of secondary crust added to Mars is estimated to be about 30 km (ref. 40). We use a conservative extrusive/intrusive ratio of 1/2, such that the amount of extrusive volcanics in a model run would equate to a 10-km-thick layer if it were evenly spread over the grid. This leads to values of $A = 1.38 \times 10^{-4}$ and $b = -1.62 \times 10^{-27}$ for calculating T in metres per year.

Code availability. We have opted not to make the code for the three-dimensional box model available, because it was written solely for this project and does not have broad utility for other analyses.

Data availability. The data that support the findings of this study are available from the corresponding author on reasonable request.

31. Agee, C. B. *et al.* Unique meteorite from early Amazonian Mars: water-rich basaltic breccia Northwest Africa 7034. *Science* **339,** 780–785 (2013).
32. Pieters, C. M. Strength of mineral absorption features in the transmitted component of near-infrared reflected light: first results from RELAB. *J. Geophys. Res.* **88,** 9534–9544 (1983).

33. Clark, R. N., Swayze, G. A., Gallagher, A., King, T. V. V. & Calvin, W. M. The USGS digital spectral library 93–592 (US Geol. Surv. Open File Rep., 1993).
34. Hartmann, W. K. Martian cratering 8: isochron refinement and the chronology of Mars. *Icarus* **174,** 294–320 (2005).
35. Robbins, S. J., Hynek, B. M., Lillis, R. J. & Bottke, W. F. Large impact crater histories of Mars: the effect of different model crater age techniques. *Icarus* **225,** 173–184 (2013).
36. Croft, S. K. The scaling of complex craters. *J. Geophys. Res. Solid Earth* **90,** C828–C842 (1985).
37. Garvin, J. B., Sakimoto, S. E., Frawley, J. J. & Schnetzler, C. North polar region craterforms on Mars: geometric characteristics from the Mars orbiter laser altimeter. *Icarus* **144,** 329–352 (2000).
38. Abramov, O., Wong, S. M. & Kring, D. A. Differential melt scaling for oblique impacts on terrestrial planets. *Icarus* **218,** 906–916 (2012).
39. Robbins, S. J. & Hynek, B. M. A new global database of Mars impact craters ≥1 km: 2. Global crater properties and regional variations of the simple-to-complex transition diameter. *J. Geophys. Res. Planet.* **117,** E06001 (2012).
40. Morschhauser, A., Grott, M. & Breuer, D. Crustal recycling, mantle dehydration, and the thermal evolution of Mars. *Icarus* **212,** 541–558 (2011).

100 μm
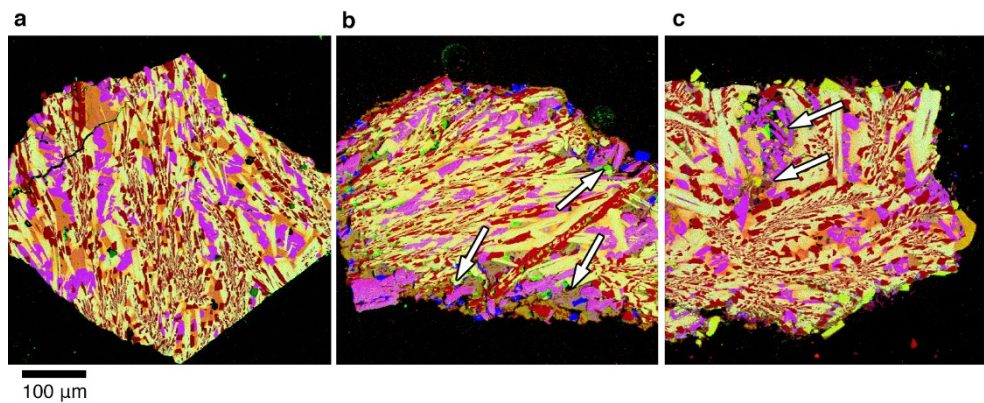
Extended Data Figure 1 | Elemental maps of basalt grain cross-sections. Electron-probe microanalyser (EPMA) chemical maps, with silicon mapped as red, aluminium as green and calcium as blue. **a**, An unaltered sample, where plagioclase appears yellow, pyroxene is purple, olivine is red and glass is orange. **b**, A sample altered in the liquid field (325 °C, 300 bar), where a thick rind of altered material (arrows) is observed (blue phase, portlandite: a calcium hydroxide). **c**, A sample altered in the supercritical field with H_2O only (425 °C, 300 bar). Alteration can be seen to extend into the interior of the grain (arrows).
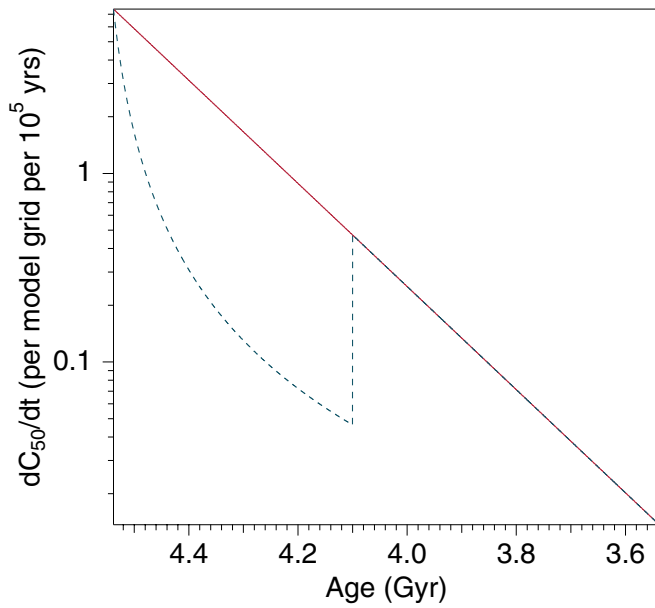
Extended Data Figure 2 | Model impact fluxes. The blue dashed line represents a sawtooth LHB with a dynamic instability occurring at 4.1 Ga (ref. 20); the solid red line represents an accretionary tail bombardment. The accretionary tail curve was found by fitting an exponential function through the N_{50} ages of the five large basins from ref. 35, then scaling to reproduce the correct number of craters for our model grid size (see Methods). The LHB curve was modelled after that in ref. 20. Here, dC_{50}/dt refers to the number of craters of diameter 50 km or more that are formed per time step over the model grid.
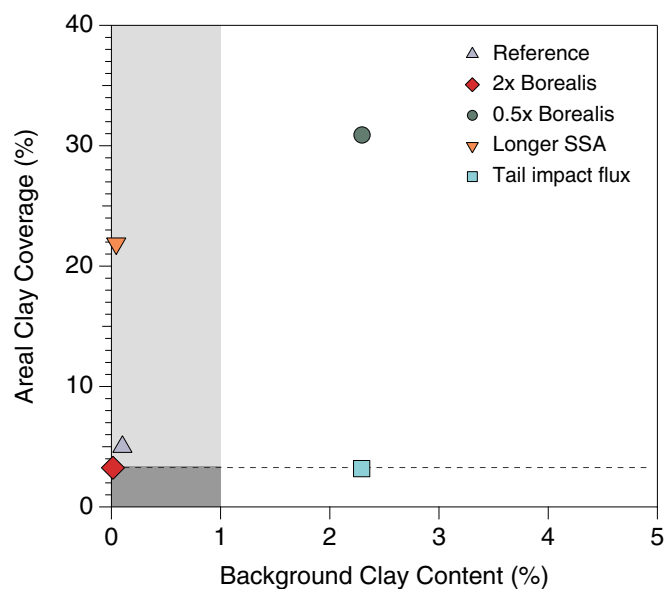
Extended Data Figure 3 | Model result metrics for surface clay content.
The areal clay coverage represents the fraction of surface grid cells with
more than 10% clay, assumed to be detectable by orbital remote sensing.
The background clay content is the median clay content in surface grid
cells located outside of detections. The dashed line at 3.4% areal clay
coverage corresponds to the estimate in ref. 4. The light shaded region
represents background clay contents of less than 1%, consistent with the
lack of detectable clay in X-ray diffraction measurements from Gale crater
soils[22], and with the lack of clays in Martian regolith breccias[23]. The dark
shaded region represents the confluence of these two constraints, such that
model results within or near this region are more consistent with observed
clay distributions on the Martian surface.

Extended Data Table 1 | Impactor list for reference model run

Crater final diameter (km)	Total number of craters	Number of craters after 4.0 Ga
50	1490	126
60	1016	82
70	663	68
80	503	46
90	371	36
100	278	30
115	246	22
130	179	17
150	122	10
170	94	10
200	57	7
250	34	3
300	33	4
350	24	3
400	13	3
450	9	1
500	10	1
600	9	1
700	1	0
800	3	1
900	2	0
1000	0	0
1100	0	0
1200	1	0
1300	1	0
1400	0	0
1500	0	0

The numbers of each crater size in the reference model run are listed for the entire duration of the run (4.538 Ga to 3.538 Ga; 'Total number of craters'), and for the period from 4.000 Ga to 3.538 Ga ('Number of craters after 4.0 Ga'). Craters are chosen randomly with probabilities from a power-law size/frequency distribution (slope $= -2.2$), with fluxes shown in Extended Data Fig. 2. Corresponding N_{50} and N_{200} values for a 4.0-Ga surface in this model run would be 33 and 2, respectively (not including craters formed after 3.538 Ga).